



Ultra-broadband optical amplification using nonlinear integrated waveguides

Downloaded from: <https://research.chalmers.se>, 2025-04-22 07:53 UTC

Citation for the original published paper (version of record):

Zhao, P., Shekhawat, V., Girardi, M. et al (2025). Ultra-broadband optical amplification using nonlinear integrated waveguides. Nature. <http://dx.doi.org/10.1038/s41586-025-08824-3>

N.B. When citing this work, cite the original published paper.

Ultra-broadband optical amplification using nonlinear integrated waveguides

<https://doi.org/10.1038/s41586-025-08824-3>

Received: 25 September 2024

Accepted: 20 February 2025

Published online: 09 April 2025

Open access

 Check for updates

Ping Zhao^{1,2✉}, Vijay Shekawat¹, Marcello Girardi¹, Zonglong He¹, Victor Torres-Company¹ & Peter A. Andrekson^{1✉}

Four-wave mixing is a nonlinear optical phenomenon that can be used for wideband low-noise optical amplification and wavelength conversion. It has been extensively investigated for applications in communications¹, computing², metrology³, imaging⁴ and quantum optics⁵. With its advantages of small footprint, large nonlinearity and dispersion-engineering capability, optical integrated waveguides are excellent candidates for realizing high-gain and large-bandwidth four-wave mixing for which anomalous dispersion is a key condition. Various waveguides based on, for example, silicon, aluminium gallium arsenide and nonlinear glass have been studied^{6–10}, but suffer from considerable gain and bandwidth reductions, as conventional design approaches for anomalous dispersion result in multi-mode operation. We present a methodology for fabricating nonlinear waveguides with simultaneous single-mode operation and anomalous dispersion for ultra-broadband operation and high-efficiency four-wave mixing. Although we implemented this in silicon nitride waveguides, the design approach can be used with other platforms as well. By using higher-order dispersion, we achieved unprecedented amplification bandwidths of more than 300 nm in these ultra-low-loss integrated waveguides. Penalty-free all-optical wavelength conversion of 100 Gbit s^{−1} data in a single optical channel of over 200 nm was realized. These single-mode dispersion-engineered nonlinear waveguides could become practical building blocks in various nonlinear photonics applications.

With the distinct advantages of overcoming the bandwidth, noise figure and wavelength range of a stimulated-emission optical amplifier and generating waves beyond those achievable with conventional lasers, four-wave mixing (FWM) has led to numerous applications in various fields. In particular, hyper-dispersion engineering (second- and fourth-order dispersion in tandem) is very critical for broadband FWM with parametric gain, which is being pursued in various areas, such as ultra-long-haul transmission¹¹, all-optical high-speed signal processing¹², light detection and ranging¹³, and biochemistry analysis¹⁴. Since the invention of low-loss silica fibres, which offer long nonlinear optical interaction distances, fibre-based FWM has been intensively investigated¹⁵. However, the fibres exhibit low nonlinearity as well as a narrow parametric bandwidth and suffer from polarization and dispersion drifts, which reduce both FWM efficiency and bandwidth¹⁶. Because of their high nonlinearity, small footprint and flexible patterning, $\chi^{(3)}$ -based nonlinear integrated waveguides provide excellent on-chip control of the optical field properties, such as dispersion and polarization state, potentially paving the way to high-efficiency and wideband FWM¹⁷. Nonlinear semiconductor integrated waveguides with a low refractive index contrast formerly attracted much interest for use in FWM but suffer from limited dispersion engineering and severe interference from other nonlinear effects¹⁸. Advances in deposition and bonding have enabled the creation of high-refractive-index-contrast nonlinear integrated waveguide structures with silica cladding that

offer strong field confinement and dispersion engineering¹⁹ and are ideally suited for broadband parametric signal processing. Many kinds of such nonlinear platforms have been explored, including silicon^{6,20,21}, silicon nitride^{22–24}, aluminium gallium arsenide^{7,25,26}, nonlinear glasses^{9,10} and graphene²⁷. In particular, a continuous-wave optical parametric gain due to FWM was achieved for the first time recently in nonlinear Si₃N₄ integrated waveguides, due to a balance of propagation loss, nonlinearity, power handling ability and dispersion engineering²², which also corresponds to high conversion efficiencies (the power ratio of the output idler to input signal).

For pump-degenerate FWM, a strong pump wave (p) and a weak signal wave (s) were passed into a $\chi^{(3)}$ -based nonlinear optical medium, where the signal was amplified and an idler wave was generated at an angular frequency of $\omega_i = 2\omega_p - \omega_s$, as illustrated in Fig. 1c. The phase mismatch parameter $\Delta K = \sum_{k=1}^{\infty} 2\beta_{2k}\Delta\omega^{2k}/(2k)! + 2\gamma P$ affects the gain, conversion efficiency and bandwidth. Here β_i is the i th-order derivative with respect to the angular frequency ω of the optical propagation constant β evaluated at the pump frequency, γ is the nonlinear coefficient, $\Delta\omega$ is the angular frequency difference between the pump and signal waves and P is the pump power²⁸. Anomalous dispersion ($\beta_2 < 0$) is of vital importance for realizing phase matching ($\Delta K = 0$) for high parametric gain and wide bandwidth, as can be seen in the Supplementary Information. However, conventional high-index-contrast silica-clad nonlinear integrated waveguides are multi-mode to achieve

¹Photonics Laboratory, Department of Microtechnology and Nanoscience, Chalmers University of Technology, Gothenburg, Sweden. ²College of Electronics and Information Engineering, Sichuan University, Chengdu, China. ✉e-mail: zhao.ping@scu.edu.cn; peter.andrekson@chalmers.se

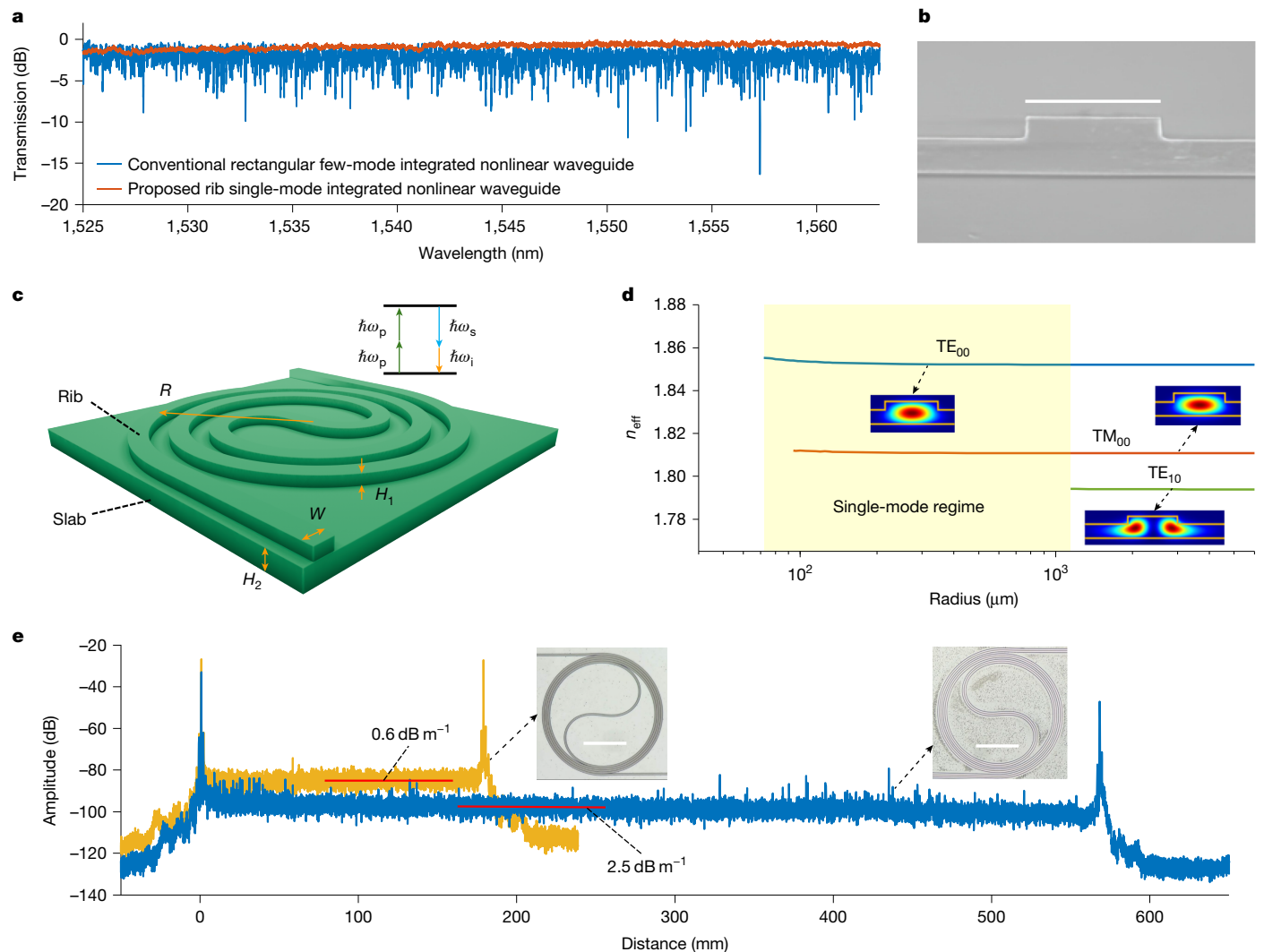


Fig. 1 | Single-mode dispersion-engineered nonlinear integrated waveguides for ultra-broadband optical amplification and wavelength conversion.

a, Normalized measured transmission spectra of a conventional rectangular-core (blue) and a proposed single-mode rib (red) nonlinear Si_3N_4 integrated waveguide. The fabrication of the few-mode rectangular-core nonlinear spiral Si_3N_4 integrated waveguide was optimized to reduce sidewall roughness. The wavelength tuning step in the measurements was 1 pm. Both waveguides were about 50 cm long. **b**, Scanning electron microscope image of the cross section of one proposed single-mode nonlinear rib Si_3N_4 integrated waveguide. **c**, Schematic diagram of one unit of the proposed spiral single-mode dispersion-engineered rib nonlinear integrated waveguide. The maximum bend radius in the spiral area was controlled to simultaneously achieve single-mode operation

and anomalous dispersion. Several spiral units were concatenated to generate a metres-long nonlinear integrated waveguide. The cladding was SiO_2 . **d**, Effective refractive index (n_{eff}) of different modes in a nonlinear rib Si_3N_4 integrated waveguide versus the bend radius, with $W = 1.9 \mu\text{m}$, $H_1 = 300 \text{ nm}$ and $H_2 = 500 \text{ nm}$. The blue, red and green lines are for the TE_{00} , TM_{00} and TE_{10} modes, respectively. Insets, intensity profiles of the different modes. The yellow lines are the SiO_2 - Si_3N_4 boundaries. **e**, OFDR traces of 18-cm-long (yellow, WG1) and 56-cm-long (blue, WG2) single-mode nonlinear rib Si_3N_4 integrated waveguides when the wavelength was scanned from 1,480 nm to 1,640 nm. The minimal propagation losses of WG1 and WG2 were 0.6 dB m^{-1} and 2.5 dB m^{-1} (red lines). Insets, optical microscope images of one spiral unit of WG1 and WG2 on two wafers, respectively. Scale bars, $1.9 \mu\text{m}$ (**b**), 0.3 mm (**e**).

anomalous dispersion^{6,7,10,22,23}, but the focus has only been on the transverse cross-sectional geometry of the waveguide. Consequently, random and unavoidable modal coupling results in power drops for both the signal and pump waves, which not only decreases the FWM gain, conversion efficiency and bandwidth but also distorts the modulated signals²⁹. For instance, the blue curve in Fig. 1a is the measured normalized transmission spectrum of a conventional rectangular-core dispersion-engineered nonlinear Si_3N_4 integrated waveguide whose fabrication was optimized to reduce the sidewall roughness. This waveguide was 2,000 nm wide, 690 nm high and about 50 cm long and supported four modes in transverse electric polarization. As can be seen in Fig. 1a, this typical conventional nonlinear Si_3N_4 integrated waveguide suffers from serious spectral fluctuations (power fading at some wavelengths of more than 10 dB) due to random mode coupling.

Single-mode $\chi^{(3)}$ -based high-index-contrast silica-clad nonlinear integrated waveguides with simultaneous anomalous dispersion are in great need for FWM but have not been reported so far. Moreover, hyper-dispersion engineering (β_4 in tandem with β_2) is quite important for ultimately broadening the FWM bandwidth. Nevertheless, ultra-broadband FWM with high conversion efficiency assisted by hyper-dispersion engineering in single-mode nonlinear waveguides has not yet been demonstrated.

We propose a universal design method for achieving anomalous-dispersion single-mode nonlinear integrated waveguides to address the above issues. The method combines longitudinal bending with a transverse cross-sectional construction. The red curve in Fig. 1a is the measured transmission spectrum of one waveguide that we designed and fabricated (Methods). It has an excellent single-mode

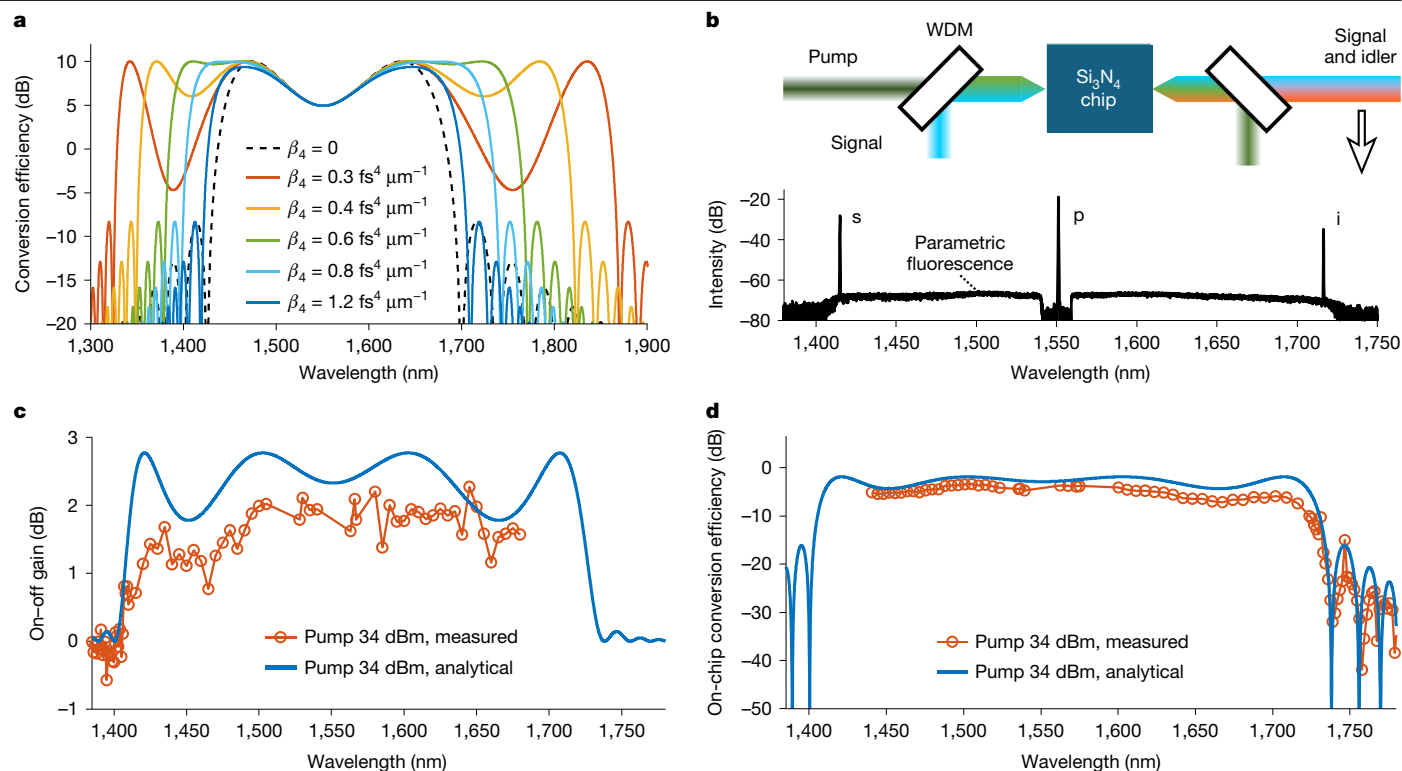


Fig. 2 | Ultra-broadband integrated parametric waveguides with hyper-dispersion engineering. **a**, Theoretical conversion-efficiency spectral curves of 1-m-long $\chi^{(3)}$ -base nonlinear integrated waveguides with various fourth-order dispersions. The waveguide loss was 1 dB m^{-1} , the nonlinear coefficient was $0.7 \text{ W}^{-1} \text{ m}^{-1}$ and the second-order dispersion was $-1 \text{ ps}^2 \text{ km}^{-1}$. The power at 1,550 nm wavelength was 35 dBm. The red, yellow, green, light blue and dark blue solid lines are for $\beta_4 = 0.3, 0.4, 0.6, 0.8$ and $1.2 \text{ fs}^4 \mu\text{m}^{-1}$, respectively. The black dashed line corresponds to the case where fourth-order dispersion is not

property in contrast to the conventional rectangular-core nonlinear integrated waveguide. Rib waveguides with silica cladding are used to achieve fewer guiding modes and lower propagation losses compared to rectangular-core waveguides with the same width and total thickness^{19,30,31}.

Figure 1b is a scanning electron microscope image of the cross section of a proposed 1.9- μm -wide single-mode nonlinear rib Si_3N_4 integrated waveguide. The key technique for simultaneously achieving single-mode operation and anomalous dispersion is to bend the waveguide to cut off higher-order modes and maintain the anomalous dispersion. Figure 1c is a schematic diagram of the proposed waveguide. W , R , H_1 and H_2 are the rib width, radius, height and slab thickness, respectively. To verify the proposed method, we used the Si_3N_4 integrated platform as an example to realize single-mode dispersion-engineered nonlinear waveguides for parametric gain. Figure 1d presents the simulated effective refractive index (n_{eff}) of different modes as a function of waveguide radius at wavelength 1,550 nm. In the simulation, the nonlinear rib Si_3N_4 waveguide was 1.9 μm wide with $H_1 = 300 \text{ nm}$ and $H_2 = 500 \text{ nm}$. The blue and red lines correspond to the fundamental transverse-electric and transverse-magnetic modes. As can be seen in Fig. 1d, when it is straight, this nonlinear rib Si_3N_4 waveguide supports three modes. When the radius was reduced to less than 1,150 μm , the high-order mode TE_{10} (green line) was cut off. Hence, with the right bend arrangement, we obtained a nonlinear spiral-rib Si_3N_4 waveguide with a single mode per polarization. Extended Data Fig. 1 presents the simulated effective refractive index versus wavelength. The cutoff wavelength of the TE_{10} mode was 1,180 nm for a bending radius of 400 μm . We show in the Supplementary Information how the propagation of the

considered. **b**, Top, experimental set-up for the FWM characterization of the 0.56-m-long single-mode nonlinear rib Si_3N_4 integrated waveguide. Bottom, spectrum after the WDM coupler with a 1,551.1 nm pump and a 1,415 nm signal. **c,d**, Measured (red circles) on-off parametric gain (**c**) and on-chip conversion efficiency (**d**) of the single-mode nonlinear Si_3N_4 integrated waveguide with a 34-dBm on-chip pump power. The solid blue curves were calculated analytically with the assumption of a spectrally constant waveguide loss of 2.5 dB m^{-1} .

TE_{00} and TE_{10} modes was affected by bending. With a larger nonlinear coefficient than the TM_{00} mode, we used the TE_{00} mode for FWM. The TE_{00} mode dispersion at 1,550 nm could become anomalous and tuned by changing the waveguide width and radius (Extended Data Fig. 2a,b).

For the fabrication tolerance analysis, Extended Data Fig. 2c,d presents the second- and fourth-order dispersion for small rib dimensions. Moreover, Fig. 1e shows the traces of optical frequency-domain reflectometry (OFDR) of two TE_{00} -mode-coupled 1.9- μm -wide nonlinear spiral-rib Si_3N_4 integrated waveguides with lengths of 18 cm (yellow, WG1) and 56 cm (blue, WG2). The slab widths of WG1 and WG2 were sufficiently large such that the TE_{00} mode was not affected by the slab sidewall and did not couple to adjacent rib waveguides (Supplementary Information). The red line in Fig. 1e indicates that the measured propagation loss of WG1 was 0.6 dB m^{-1} . For WG2, the propagation loss was about 2.5 dB m^{-1} . The insets in Fig. 1e are optical microscope images of WG1 and WG2, respectively. One can see that WG2 suffered from residual nanoparticles of which WG1 was almost free. The propagation loss difference between WG1 and WG2 was mainly due to fabrication variation, which we are trying to improve. We fabricated six 56-cm-long single-mode nonlinear rib Si_3N_4 integrated waveguides. WG2 was the only one without large defects on the OFDR traces. The yield for the 18-cm-long rib waveguides was 4/20, which was mainly limited by the misalignment of the dual-layer tapers and minor defects.

Apart from the single-mode waveguiding property, we investigated how the hyper-dispersion engineering ultimately extended the bandwidth of the FWM-based parametric process. Figure 2a depicts the theoretical conversion-efficiency spectra of a 1-m-long nonlinear integrated waveguide with a pump power of 35 dBm at 1,550 nm. In the

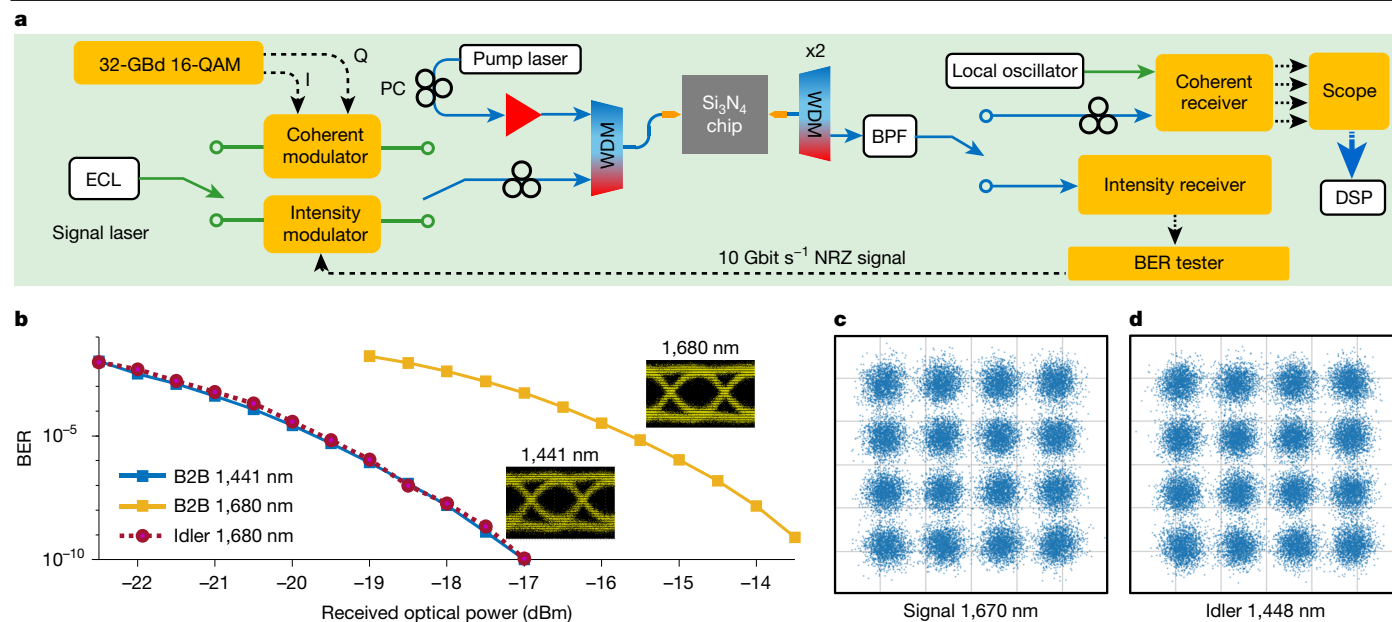


Fig. 3 | Ultra-broadband high-efficiency, high-speed all-optical wavelength conversion based on single-mode nonlinear spiral-rib Si_3N_4 integrated waveguides. **a**, Experimental set-up of the Si_3N_4 -chip-based all-optical wavelength conversion for both intensity modulation and coherent optical communications. The on-chip pump power was 34 dBm. **b**, BER as a function of received optical power of 10 Gbit s^{-1} NRZ signals (1,680 nm) and converted

idlers (1,441 nm, purple dashed line). Insets, eye diagrams of the B2B optical signals at wavelengths of 1,441 nm and 1,680 nm, respectively. **c, d**, Constellation diagrams for a 1,670-nm signal (**c**) and a 1,448-nm idler (**d**) with 32-GBd 16-QAM after offline digital signal processing (DSP). BPF, band-pass filter; PC, polarization controller.

calculation, the second-order dispersion was $-1 \text{ ps}^2 \text{ km}^{-1}$ at 1,550 nm, the effective nonlinear coefficient was $0.7 \text{ W}^{-1} \text{ m}^{-1}$ and the waveguide loss was 1 dB m^{-1} . The maximum conversion efficiency was 10 dB, which corresponds to a maximum parametric gain of about 10 dB for the signal wave³². The parametric gain spectrum was like the spectral curve for conversion efficiency in this case. The black dashed line is for $\beta_4 = 0$ for which the amplification bandwidth was 270 nm. The red, yellow, green and blue solid lines are for $\beta_4 = 0.3, 0.4, 0.6$ and $1.2 \text{ fs}^4 \mu\text{m}^{-1}$, respectively. As shown by Fig. 2a, the amplification bandwidth increased to 542 nm for $\beta_4 = 0.3 \text{ fs}^4 \mu\text{m}^{-1}$, as the fourth-order dispersion led to new phase-matching wavelengths²⁸. When the balance among the nonlinear shift, second- and fourth-order dispersion was achieved with $\beta_4 = 0.6 \text{ fs}^4 \mu\text{m}^{-1}$, two flat gain regimes were obtained. The amplification bandwidth reached 385 nm (43% bandwidth increase compared to $\beta_4 = 0$). Hence, fourth-order dispersion plays a vital role in realizing ultra-wideband parametric devices.

Furthermore, we characterized the ultra-broadband FWM in WG2 using continuous-wave pump–probe approaches based on the experimental diagram in Fig. 2b (Methods). The on-chip pump power was 34 dBm considering the coupling loss. The lower part of Fig. 2b shows the output optical spectrum of WG2 with the residual pump mitigated by a wavelength-division multiplexing (WDM) coupler. The signal, pump and idler wavelengths were 1,415, 1,551.1 and 1,716 nm, respectively. Ultra-wideband flat parametric fluorescence during FWM was also observed, as can be seen in Fig. 2b. Figure 2c, d depicts the measured (blue) on–off parametric gain and on-chip conversion-efficiency spectra, respectively. The on–off gain was used as it can mitigate the impact of the wavelength-dependent coupling loss of the tapers on the measurements. The solid lines are theoretically fitted spectra with $\beta_2 = -2.2 \text{ ps}^2 \text{ km}^{-1}$ and $\beta_4 = 1.9 \text{ fs}^4 \mu\text{m}^{-1}$ at 1,551 nm. The measured and theoretical curves are in good agreement with small discrepancies, which may be due to the wavelength-dependent loss of the waveguide. The on-chip waveguide loss in the L band was about 1 dB, indicating that we achieved an on-chip net continuous-wave parametric gain of 1 dB. Besides, we obtained a maximum on-chip conversion efficiency

of -3.4 dB at 1,500-nm wavelength, as shown in Fig. 2d. The gain and conversion-efficiency spectra in Fig. 2c, d indicate that we realized a FWM bandwidth of 330 nm—one of the widest bandwidths of all reported continuous-wave optical amplifiers to date. As there were not enough lasers to cover the full FWM bandwidth during the measurements, we recorded the pure parametric-fluorescence spectrum as a measure of the parametric gain profile, which changed with the dispersion by adjusting the pump wavelength (Supplementary Information). Moreover, the fitted second- and fourth-order dispersion agreed with the waveguide design, as we can see from Extended Data Fig. 2c, d, which verifies that the nonlinear Si_3N_4 integrated platform is very tolerant to fabrication uncertainties. β_2 was more sensitive to variations in the thickness, whereas β_4 exhibited a larger tolerance to dimension variations, as can be seen from Extended Data Fig. 2c, d. The fitted β_2 is slightly smaller than the designed value of $-4 \text{ ps}^2 \text{ km}^{-1}$, which is mainly attributed to the thickness variation of the waveguide. Si_3N_4 wafers will be planarized to improve the thickness uniformity³³.

Furthermore, we applied the Si_3N_4 -chip ultra-broadband efficient FWM to all-optical high-speed wavelength conversion for communications. Figure 3a shows the experimental set-up with intensity and coherent modulation (Methods). We used 10 Gbit s^{-1} non-return-to-zero (NRZ) intensity modulation to check the impairments to the idler quality during wavelength conversion. Figure 3b presents the bit-error rate (BER) of the back-to-back (B2B) 1,441 nm signal (blue solid line), 1,680 nm signal (yellow solid line) and 1,441 nm idler (purple dotted line). The B2B BER difference between 1,441 and 1,680 nm signals was due to the wavelength-dependent responsivity of the intensity receiver. As can be seen in Fig. 3b, the idler suffered negligible penalty compared to the 1,441 nm B2B signal, which indicates that the proposed CMOS-compatible single-mode nonlinear Si_3N_4 integrated waveguide is promising for all-optical signal processing. In addition, we implemented the all-optical wavelength conversion of single-polarization 32-GBd 16-quadrature-amplitude-modulation (16-QAM) signals with a net rate over 100 Gbit s^{-1} , based on the 56-cm-long single-mode nonlinear Si_3N_4 integrated waveguide. Figure 3c, d show the constellation

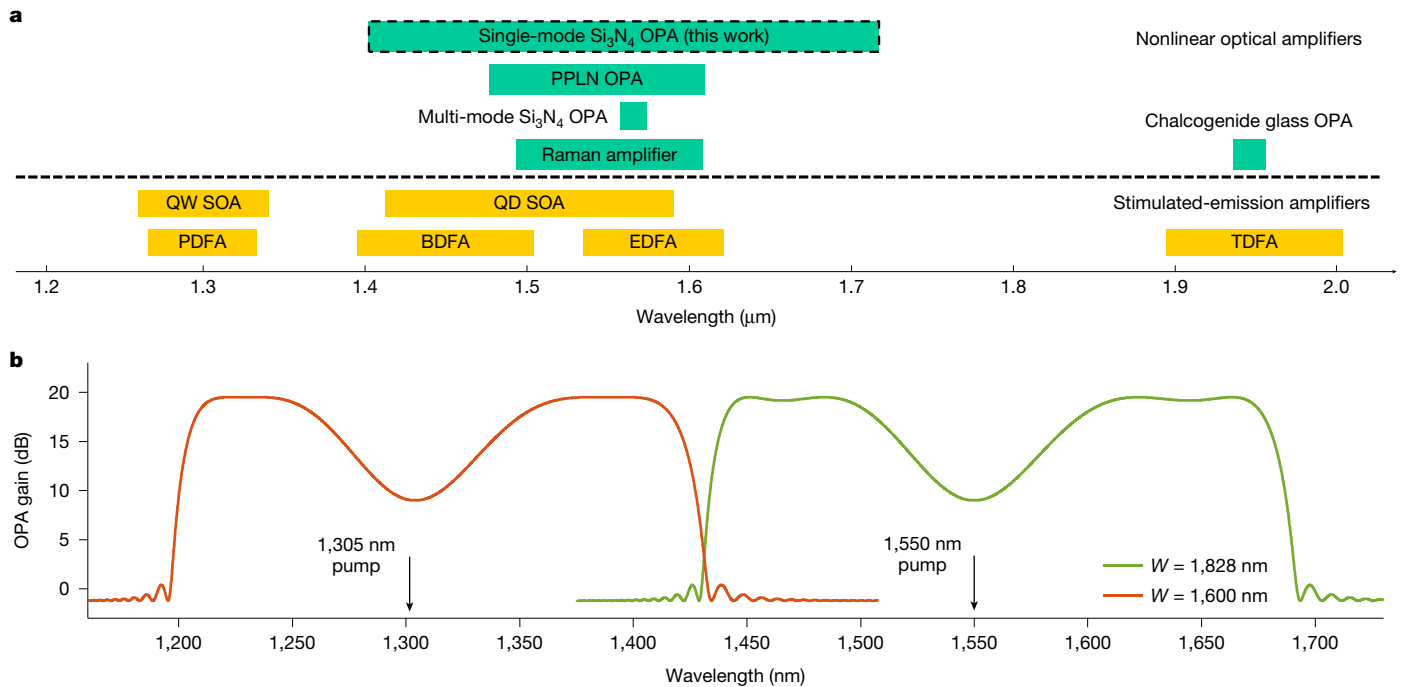


Fig. 4 | Bandwidth and wavelength ranges of different optical amplifiers.

a, State-of-the-art bandwidth of continuous-wave optical amplification in the near-infrared regime based on both stimulated-emission and nonlinear optical platforms. **b**, Theoretical gain spectra of OPAs based on optimized single-mode nonlinear rib Si_3N_4 integrated waveguides pumped at wavelengths of 1,305 nm (red) or 1,550 nm (green). Both Si_3N_4 waveguides have the same rib and slab thicknesses ($H_1 = 300$ nm and $H_2 = 500$ nm) and can be integrated on the same

wafer but for different widths of 1,600 nm and 1,828 nm. The waveguide lengths are 2 m with an assumed propagation loss of 0.6 dB m^{-1} . BDFA, bismuth-doped fibre amplifier; EDFA, erbium-doped fibre amplifier; PDFA, praseodymium-doped fibre amplifier; PPLN, periodically poled lithium niobate; QD, quantum dot; QW, quantum well; SOA, semiconductor optical amplifier; TDFA, thulium-doped fibre amplifier.

diagrams for the B2B 1,670-nm signal and converted 1,448-nm idler, respectively. We have realized all-optical wavelength conversion for a more than 200-nm-wide wavelength span at 100 Gbit s^{-1} without amplifying the signal and idler waves. As the 32-GBd 16-QAM is the dominant modulation format of current optical-fibre communication systems connecting the continents on Earth, the Si_3N_4 -chip high-efficiency wavelength conversion demonstrated has a bright future in the all-optical reconfiguration of global WDM optical networks by unlocking transmission beyond the C and L bands of optical fibres³⁴ and increasing the capacity of optical neuromorphic computing for artificial intelligence³⁵.

Figure 4a summarizes the bandwidth of various types of wideband continuous-wave optical amplifiers. Various material platforms have been developed for stimulated-emission optical amplifiers, such as erbium-doped fibre amplifiers³⁶, bismuth-doped fibre amplifiers³⁷, thulium-doped fibre amplifiers for optical applications³⁸, praseodymium-doped fibre amplifiers³⁹, and quantum-well and quantum-dot semiconductor optical amplifiers^{40,41}. To cover the entire transmission windows of telecommunication-grade silica and widely studied hollow-core fibres⁴², new stimulated-emission materials with different bandgaps need to be investigated and developed. On the other hand, nonlinear optical effects, including the Raman effect⁴³, difference-frequency generation and FWM, have also been applied to build wideband optical amplifiers based on single material such that the operating wavelength can be flexibly tuned by changing the pump frequency and the waveguide dispersion. Amplifiers based on the difference-frequency or FWM effects are also called optical parametric amplifiers (OPAs). Periodically poled lithium niobate waveguide OPAs based on the difference-frequency effect have been investigated⁴⁴, leading to ultra-high-speed optical-fibre transmission beyond conventional telecommunication bands⁴⁵. Based on the FWM process, OPAs using $\chi^{(3)}$ -nonlinear nanophotonic waveguides are free of complicated periodic poling. Continuous-wave nanophotonic OPAs were first realized

with chalcogenide glass microfibres with a gain bandwidth of about 20 nm (ref. 46). Our single-mode nonlinear rib $\chi^{(3)}$ integrated waveguides, which have more freedom in dispersion engineering, enabled us to demonstrate an OPA bandwidth of 330 nm (Fig. 4a), which is wider than that of previously published continuous-wave optical amplifiers. At present, the length of the fabricated $1.9\text{-}\mu\text{m}$ -wide single-mode nonlinear spiral-rib Si_3N_4 integrated waveguide greatly limits the parametric gain. We are continuing to optimize the fabrication and believe that the yield of long ultra-low-loss single-mode nonlinear rib Si_3N_4 waveguides can be improved. The length issue together with the yield may not be problematic for CMOS foundries, as their deep-ultraviolet exposure technologies are mature for massive nanofabrication.

We theoretically optimized the width of the single-mode nonlinear rib Si_3N_4 integrated waveguide for high-gain OPAs. Figure 4b shows the theoretical parametric gain spectra of 2-m-long 0.6 dB m^{-1} -loss single-mode nonlinear rib Si_3N_4 integrated waveguides with widths of 1,600 nm (red) and 1,828 nm (green) and a pump power of 34 dBm. Both waveguides have the same rib thickness ($H_1 = 300$ nm) and slab thickness ($H_2 = 500$ nm) and can be integrated on the same wafer, potentially with a total chip size of $3 \text{ cm} \times 3 \text{ cm}$. As can be seen in Fig. 4b, the two OPAs, for which the pump wavelengths are 1,305 and 1,550 nm, provide a maximum gain of about 20 dB and cover the whole transmission window of single-mode telecommunication fibres. We also analysed the fabrication tolerance of the high-gain Si_3N_4 waveguide OPA (Supplementary Information). With the advances in semiconductor optoelectronics, continuous-wave pump lasers operating at wavelengths of 1,305 and 1,550 nm with watt-level power could also become available⁴⁷ and may lead to compact OPAs based on hybrid photonic integration⁴⁸. The spectral flatness of the OPA over the 200-nm bandwidth could be improved by dual-pump, dispersion or pump-phase shifting techniques that can be implemented in integrated waveguide platforms^{49,50}. A rib structure with several layers would provide more degrees of freedom

for hyper-dispersion engineering and may lead to a broader parametric bandwidth, which is yet to be explored.

In this paper, we proposed and demonstrated extremely low-loss single-mode nonlinear Si_3N_4 integrated waveguides with hyper-dispersion engineering for ultra-broadband, efficient, continuous-wave FWM. Unlike conventional approaches focusing on the waveguide cross section, we exploited the three-dimensional waveguide geometry for on-chip optical field manipulation, simultaneously achieving single-mode transmission and dispersion engineering of nonlinear integrated nanophotonic waveguides in telecommunication bands. Using the 0.56-m-long single-mode nonlinear rib Si_3N_4 integrated waveguide with hyper-dispersion engineering, we obtained a continuous-wave gain bandwidth of 330 nm in the near-infrared regime. The whole transmission window of telecommunication silica fibres could potentially be covered by the parametric gain profiles of single-mode nonlinear rib Si_3N_4 waveguides integrated on the same wafer. Furthermore, we realized wide all-optical wavelength conversion of single-wavelength signals beyond 100 Gbit s^{-1} without amplifying the signal and idler wave. These experimental results agree with theoretical expectations. A higher continuous-wave parametric gain and conversion efficiency could be expected with longer low-loss single-mode nonlinear rib Si_3N_4 integrated waveguides. With the combination of cross-sectional shaping and longitudinal bending, the waveguide design technique we proposed is easy to implement. It could allow other integrated platforms to realize low-loss single-mode dispersion-engineered nonlinear waveguides that could become key building blocks for optics, making the technique promising, from fundamental research in photonics, physics, quantum physics, chemistry and biology to industrial applications in communications, computing, spectroscopy, imaging and metrology.

Online content

Any methods, additional references, Nature Portfolio reporting summaries, source data, extended data, supplementary information, acknowledgements, peer review information; details of author contributions and competing interests; and statements of data and code availability are available at <https://doi.org/10.1038/s41586-025-08824-3>.

- Hansryd, J., Andrekson, P. A., Westlund, M., Jie, L. & Hedekvist, P. Fiber-based optical parametric amplifiers and their applications. *IEEE J. Sel. Top. Quantum Electron.* **8**, 506–520 (2002).
- Gu, W. et al. All-optical complex-valued convolution based on four-wave mixing. *Optica* **11**, 64–72 (2024).
- Hudelst, F. et al. Quantum metrology with parametric amplifier-based photon correlation interferometers. *Nat. Commun.* **5**, 3049 (2014).
- Lemos, G. B. et al. Quantum imaging with undetected photons. *Nature* **512**, 409–412 (2014).
- Wang, J. et al. Multidimensional quantum entanglement with large-scale integrated optics. *Science* **360**, 285–291 (2018).
- Foster, M. A. et al. Broad-band optical parametric gain on a silicon photonic chip. *Nature* **441**, 960–963 (2006).
- Pu, M. et al. Ultra-efficient and broadband nonlinear AlGaAs-on-insulator chip for low-power optical signal processing. *Laser Photonics Rev.* **12**, 1800111 (2018).
- Lei, Z. et al. Over 100 nm wavelength conversion bandwidth with high efficiency on AlGaAsOI nonlinear waveguides. In *Proc. Optical Fiber Communication Conference Th1D.6* (Optica, 2024).
- Lamont, M. R. E. et al. Net-gain from a parametric amplifier on a chalcogenide optical chip. *Opt. Express* **16**, 20374–20381 (2008).
- Pasquazi, A. et al. Efficient wavelength conversion and net parametric gain via four wave mixing in a high index doped silica waveguide. *Opt. Express* **18**, 7634–7641 (2010).
- Olsson, S. L. I., Eliasson, H., Astra, E., Karlsson, M. & Andrekson, P. A. Long-haul optical transmission link using low-noise phase-sensitive amplifiers. *Nat. Commun.* **9**, 2513 (2018).
- Koos, C. et al. All-optical high-speed signal processing with silicon-organic hybrid slot waveguides. *Nat. Photon.* **3**, 216–219 (2009).
- Ishimura, S., Kan, T., Takahashi, H., Tsuritani, T. & Suzuki, M. Ultralinear 140-GHz FMCW signal generation with optical parametric wideband frequency modulation enabling 1-mm range resolution. *Opt. Express* **31**, 13384 (2023).
- Lüpken, N. M., Würthwein, T., Boller, K.-J. & Fallnich, C. Optical parametric amplification in silicon nitride waveguides for coherent Raman imaging. *Opt. Express* **29**, 10424–10433 (2021).
- Stolen, R. H., Bjorkholm, J. E. & Ashkin, A. Phase-matched three-wave mixing in silica fiber optical waveguides. *Appl. Phys. Lett.* **24**, 308–310 (1974).

- Yaman, F., Lin, Q., Radic, S. & Agrawal, G. P. Impact of dispersion fluctuations on dual-pump fiber-optic parametric amplifiers. *IEEE Photonics Technol. Lett.* **16**, 1292–1294 (2004).
- Moss, D. J., Morandotti, R., Gaeta, A. L. & Lipson, M. New CMOS-compatible platforms based on silicon nitride and Hydex for nonlinear optics. *Nat. Photon.* **7**, 597–607 (2013).
- Uskov, A., Mork, J. & Mark, J. Wave mixing in semiconductor laser amplifiers due to carrier heating and spectral-hole burning. *IEEE J. Quantum Electron.* **30**, 1769–1781 (1994).
- Soref, R. A., Schmidtchen, J. & Petermann, K. Large single-mode rib waveguides in GeSi-Si and Si-on-SiO₂. *IEEE J. Quantum Electron.* **27**, 1971–1974 (1991).
- Gajda, A. et al. Highly efficient CW parametric conversion at 1550 nm in SOI waveguides by reverse biased p-i-n junction. *Opt. Express* **20**, 13100 (2012).
- Morrison, B., Zhang, Y., Pagani, M., Eggleton, B. & Marpaung, D. Four-wave mixing and nonlinear losses in thick silicon waveguides. *Opt. Lett.* **41**, 2418–2421 (2016).
- Ye, Z. et al. Overcoming the quantum limit of optical amplification in monolithic waveguides. *Sci. Adv.* **7**, eabi8150 (2021).
- Riemensberger, J. et al. A photonic integrated continuous-travelling-wave parametric amplifier. *Nature* **612**, 56–61 (2022).
- Tan, D. T. H., Ooi, K. J. A. & Ng, D. K. T. Nonlinear optics on silicon-rich nitride—a high nonlinear figure of merit CMOS platform. *Photonics Res.* **6**, B50 (2018).
- Dolgaleva, K. et al. Tuneable four-wave mixing in AlGaAs nanowires. *Opt. Express* **23**, 22477 (2015).
- Qin, J. et al. On-chip high-efficiency wavelength multicasting of PAM3/PAM4 signals using low-loss AlGaAs-on-insulator nanowaveguides. *Opt. Lett.* **45**, 4539–4542 (2020).
- Feng, Q. et al. Enhanced optical Kerr nonlinearity of graphene/Si hybrid waveguide. *Appl. Phys. Lett.* **114**, 071104 (2019).
- Agrawal, G. P. *Nonlinear Fiber Optics* 4th edn (Elsevier, 2009).
- Zhao, P., He, Z., Shekhawat, V., Karlsson, M. & Andrekson, P. A. 100-Gbps per-channel all-optical wavelength conversion without pre-amplifiers based on an integrated nanophotonic platform. *Nanophotonics* **12**, 3427–3434 (2023).
- Marcattili, E. A. J. Bends in optical dielectric guides. *Bell Syst. Tech. J.* **48**, 2103–2132 (1969).
- Marcuse, D. *Theory of Dielectric Optical Waveguides* (Academic, 1974).
- Andrekson, P. A. & Karlsson, M. Fiber-based phase-sensitive optical amplifiers and their applications. *Adv. Opt. Photonics* **12**, 367–428 (2020).
- Ji, X. et al. Ultra-low-loss on-chip resonators with sub-milliwatt parametric oscillation threshold. *Optica* **4**, 619 (2017).
- Kong, D. et al. Super-broadband on-chip continuous spectral translation unlocking coherent optical communications beyond conventional telecom bands. *Nat. Commun.* **13**, 4139 (2022).
- Shastri, B. J. et al. Photonics for artificial intelligence and neuromorphic computing. *Nat. Photon.* **15**, 102–114 (2021).
- Mears, R. J., Reekie, L., Jauncey, I. M. & Payne, D. N. Low-noise erbium-doped fibre amplifier operating at 1.54 μm . *Electron. Lett.* **23**, 1026–1028 (1987).
- Liu, S. et al. High bismuth-doped germanosilicate fiber for efficient E + S-band amplification. *Opt. Lett.* **49**, 314 (2024).
- Li, Z. et al. Thulium-doped fiber amplifier for optical communications at 2 μm . *Opt. Express* **21**, 9289–9297 (2013).
- Ohishi, Y. et al. Pr^{3+} -doped fluoride fiber amplifier operating at 1.31 μm . *Opt. Lett.* **16**, 1747–1749 (1991).
- Michael, J. C. *Semiconductor Optical Amplifiers* (Springer, 2004).
- Akiyama, T., Sugawara, M. & Arakawa, Y. Quantum-dot semiconductor optical amplifiers. *Proc. IEEE* **95**, 1757–1766 (2007).
- Poletti, F. Nested antiresonant nodeless hollow core fiber. *Opt. Express* **22**, 23807–23828 (2014).
- Islam, M. N. Raman amplifiers for telecommunications. *IEEE J. Sel. Top. Quantum Electron.* **8**, 548–559 (2002).
- Umeki, T., Tadanaga, O. & Asobe, M. Highly efficient wavelength converter using direct-bonded PPZnLN ridge waveguide. *IEEE J. Quantum Electron.* **46**, 1206–1213 (2010).
- Kobayashi, T. et al. 103-ch. 132-Gbaud PS-QAM signal inline-amplified transmission with 14.1-THz bandwidth lumped PPLN-based OPAs over 400-km G.652.D SMF. In *Proc. Optical Fiber Communication Conference Th4B.6* (Optica, 2023).
- Xing, S. et al. Mid-infrared continuous-wave parametric amplification in chalcogenide microstructured fibers. *Optica* **4**, 643 (2017).
- Leisher, P. O. et al. >3W diffraction-limited 1550 nm diode laser amplifiers for LIDAR. In *Proc. SPIE 11982 Components and Packaging for Laser Systems VIII* 1198206 (2022).
- Liang, D., Roelkens, G., Baets, R. & Bowers, J. E. Hybrid integrated platforms for silicon photonics. *Materials* **3**, 1782–1802 (2010).
- Provino, L., Mussot, A., Lantz, E., Sylvestre, T. & Maillotte, H. Broadband and flat parametric amplifiers with a multisection dispersion-tailored nonlinear fiber arrangement. *J. Opt. Soc. Am. B* **20**, 1532–1537 (2003).
- Takasaka, S., Mimura, Y., Takahashi, M., Sugizaki, R. & Ogoshi, H. Flat and broad amplification by quasi-phase-matched fiber optical parametric amplifier. In *Proc. Optical Fiber Communication Conference OTh1C.4* (Optica, 2012).

Publisher's note Springer Nature remains neutral with regard to jurisdictional claims in published maps and institutional affiliations.



Open Access This article is licensed under a Creative Commons Attribution 4.0 International License, which permits use, sharing, adaptation, distribution and reproduction in any medium or format, as long as you give appropriate credit to the original author(s) and the source, provide a link to the Creative Commons licence, and indicate if changes were made. The images or other third party material in this article are included in the article's Creative Commons licence, unless indicated otherwise in a credit line to the material. If material is not included in the article's Creative Commons licence and your intended use is not permitted by statutory regulation or exceeds the permitted use, you will need to obtain permission directly from the copyright holder. To view a copy of this licence, visit <http://creativecommons.org/licenses/by/4.0/>.

© The Author(s) 2025

Methods

Fabrication and linear characterization of the spiral-rib waveguides

The proposed rib waveguide was manufactured by the subtractive electron-beam lithography process used for ultra-low-loss high-confinement Si_3N_4 waveguides^{51,52}. An 800-nm-thick Si_3N_4 layer was deposited by low-pressure chemical vapour deposition on a 4-inch Si wafer with 3- μm -thick SiO_2 layer on top. Two-step etching was used to fabricate the rib waveguides with dual-layer tapers at the chip edges for coupling with lensed fibres. The 300-nm-thick 1.9- μm -wide Si_3N_4 spiral rib was defined in the first etching. To prevent the Si_3N_4 from cracking, 3- μm -wide microgrooves between the rib waveguides were formed in the 500-nm-thick slab layer during the second etching. The etched waveguides were then annealed above 1,100 °C in an Ar-flow atmosphere and cladded with 3- μm -thick SiO_2 by low-pressure chemical vapour deposition. Finally, the whole wafer was diced into chips by etching. The parameters of WG1 and WG2 are listed in Extended Data Table 1. WG1 and WG2 both consist of several concatenated single-mode spiral units with 800- μm -long straight-connection rib waveguides in between. We used the adiabatic transition between the spiral and connection waveguides. Although the very short straight-connection rib waveguides supported two transverse-electric modes, more than 90% of both WG1 and WG2 operated in single mode. There are 12 and 68 spiral units in WG1 and WG2, respectively.

Lensed fibres with beam-spot diameters of 3 μm were used to couple light with the Si_3N_4 nanophotonic chip. We found that the average coupling loss was about 2.5 dB per facet at a wavelength of 1,550 nm for the TE_{00} mode of the spiral-rib Si_3N_4 waveguide. The waveguide propagation loss was measured using a commercial OFDR tester combined with a wavelength-scanning laser. For the linear transmission spectrum measurements of the Si_3N_4 waveguides, we focused on the TE_{00} mode and used a power-constant tunable laser with a wavelength step of 1 pm.

FWM characterization with single-mode nonlinear rib Si_3N_4 integrated waveguides

We used the pump-probe approach to measure the parametric gain and conversion efficiency of the continuous-wave FWM in the 0.56-m-long single-mode rib nonlinear Si_3N_4 integrated waveguide. Three semiconductor external-cavity lasers (ECLs) were used to generate a signal wave that could be tuned from 1,355 to 1,680 nm. Another semiconductor ECL emitted a 1,551.1-nm pump wave, which was amplified by a high-power erbium-doped fibre amplifier. The pump and signal waves were combined by a low-loss thin-film WDM coupler with a bandwidth of 4 nm and entered the single-mode nonlinear rib Si_3N_4 integrated waveguide through the lensed fibre. The polarization states of both the pump and signal waves were aligned to the TE_{00} mode of the rib Si_3N_4 waveguide. Then, 1% of the optical field at the Si_3N_4 waveguide input port was recorded by an optical spectrum analyser. At the Si_3N_4 waveguide output port, we used a 15-nm-wide coarse WDM coupler to mitigate the residual pump intensity before we measured the optical spectrum. Using power calibrations for the input and output optical spectra, we calculated the FWM gain and conversion efficiency for each signal wavelength.

Wavelength conversion for optical communications

Using the 0.56-m-long single-mode nonlinear rib Si_3N_4 integrated waveguide, we implemented all-optical wavelength conversion of NRZ and 16-QAM signals. The pump wavelength was 1,551.1 nm with a continuous-wave on-chip power of 34 dBm in all the measurements. No optical amplification was used in the signal or idler wave paths. The green and blue lines in Fig. 3a are for polarization-maintaining

and non-polarization-maintaining single-mode fibre patch cords, respectively.

For the NRZ modulation format, a Mach-Zehnder modulator was used to convert the 10 Gbit s⁻¹ electrical signals from a BER tester into the optical domain with a carrier wavelength of 1,680 nm. The optical power of the output signal from the Mach-Zehnder modulator was about 2 dBm. After a 10 Gbit s⁻¹ NRZ idler wave at 1,441 nm was generated during the on-chip FWM process, two coarse 1,550-nm WDM couplers with bandwidths of 15 nm were used to thoroughly mitigate the residual pump. We used a band-pass filter to select the idler wave. A 10-GHz intensity receiver with one photodetector and two radio-frequency amplifiers converted the optical signals back to the electrical domain, and these signals were fed to the BER tester and used to calculate the BER and record the eye diagrams of the received signal.

Regarding the 16-QAM optical signals, an electrical arbitrary waveform generator was used to generate the 32-GBd in-phase and quadrature components, which were amplified separately and sent to a single-polarization coherent electrical-optical modulator. To detect the 16-QAM optical signals after wavelength conversion, a commercial coherent receiver with another tunable ECL as a local oscillator was used. The signal wavelength at the chip input was set to 1,670 nm so that the 16-QAM data could be converted to a 1,447-nm idler wave such that the wavelength-dependent coherent receiver responsivity was still sufficient for data recovery. The electrical signals after the coherent receiver were recorded by a high-speed real-time scope. Offline digital signal processing was applied to analyse the signal BER and constellation.

Data availability

The data that support the findings of this study are available from the corresponding authors upon request.

51. Girardi, M. et al. Multilayer integration in silicon nitride: decoupling linear and nonlinear functionalities for ultralow loss photonic integrated systems. *Opt. Express* **31**, 31435–31446 (2023).
52. Ye, Z., Twayana, K., Andrekson, P. A. & Torres-Company, V. High-Q Si_3N_4 microresonators based on a subtractive processing for Kerr nonlinear optics. *Opt. Express* **27**, 35719–35727 (2019).

Acknowledgements We thank M. Karlsson and Y. Gao for fruitful technical discussions, E. Torres, M. Myreemark and C. Lei for their help with chip preparation and experiments, M. Pu at the Technical University of Denmark, F. Olofsson, and the Santec Corporation for sharing equipment. This work was performed in part at Myfab Chalmers. This work was partially funded by the Swedish Research Council (grant nos. VR-2015-00535 to P.A.A. and VR-2020-00453 to V.T.-C.), the K. A. Wallenberg Foundation through a KAW Scholarship (P.A.A.) and the Chinese Fundamental Research Funds for the Central Universities (grant no. YJ202478).

Author contributions P.Z. and P.A.A. were responsible for the concept. P.Z. designed the waveguide, characterized the chip, performed the theoretical modelling of the waveguides, simulated the nonlinear process, designed the waveguide layout, completed the linear and nonlinear characterization of the waveguides, and processed the data. V.S. and M.G. developed the waveguide nanofabrication process. P.Z., Z.H. and V.S. used the chip for optical transmission and implemented the wavelength conversion experiment for optical communications. V.S. fabricated the waveguides. P.A.A. and V.T.-C. acquired funding and administered the project. P.A.A. supervised the project. P.Z. and P.A.A. wrote the original draft of the manuscript. P.A.A., V.S. and V.T.-C. reviewed and edited the manuscript.

Funding Open access funding provided by Chalmers University of Technology.

Competing interests The authors declare no competing interests.

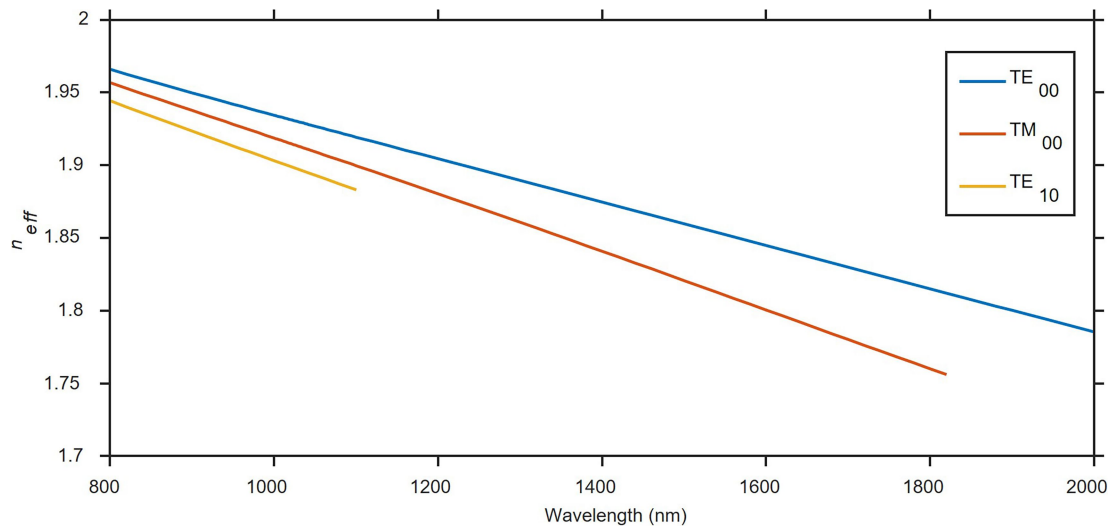
Additional information

Supplementary information The online version contains supplementary material available at <https://doi.org/10.1038/s41586-025-08824-3>.

Correspondence and requests for materials should be addressed to Ping Zhao or Peter A. Andrekson.

Peer review information Nature thanks the anonymous reviewers for their contribution to the peer review of this work. Peer reviewer reports are available.

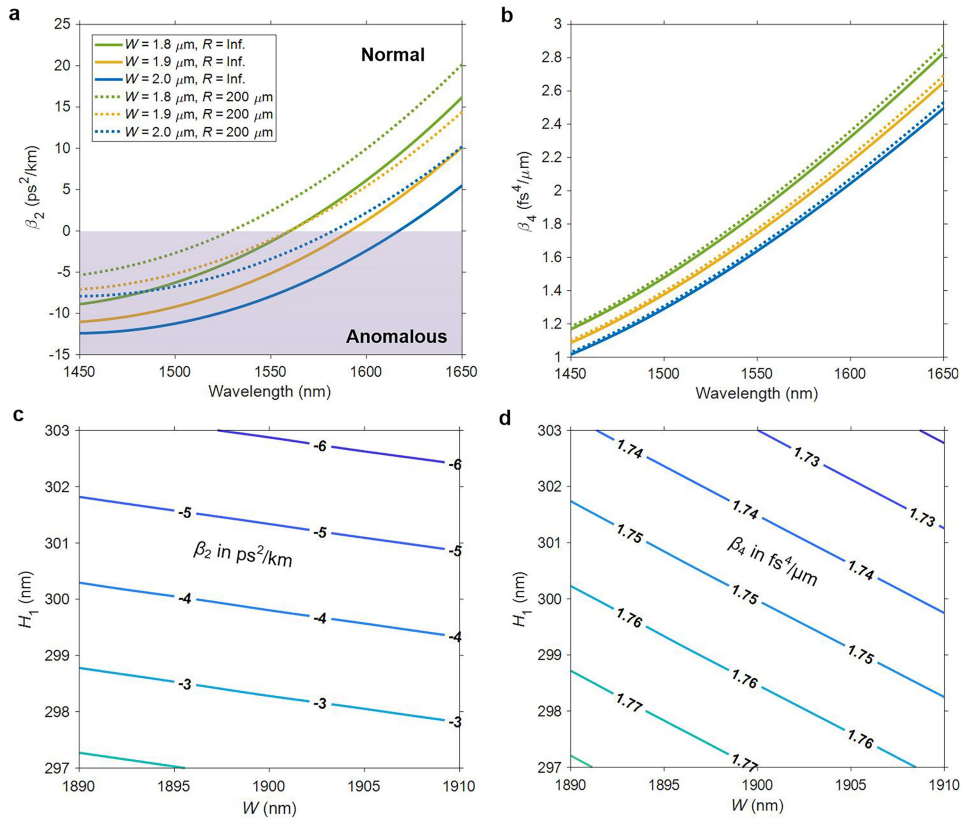
Reprints and permissions information is available at <http://www.nature.com/reprints>.



Extended Data Fig. 1 | Simulated effective refractive index varying with wavelength for a bent single-mode rib silicon nitride waveguide.

The waveguide bending radius in the simulation based on COMSOL Multiphysics is constant 400 μm with $W = 1.9 \mu\text{m}$, $H_1 = 300 \text{ nm}$ and $H_2 = 500 \text{ nm}$. As can be

seen, TE₁₀ and TM₀₀ modes are cut off at the wavelength of 1100 nm and 1820 nm, respectively. Thus, only one TE and one TM mode exists at the wavelength range studied here.



Extended Data Fig. 2 | Dispersion properties of rib Si_3N_4 nonlinear integrated waveguides. **a, b**, Second- (a) and fourth-order (b) dispersion spectra of TE_{00} mode in the proposed rib Si_3N_4 nonlinear integrated waveguides with $H_1 = 300$ nm and $H_2 = 500$ nm. The solid and dotted lines correspond to cases of straight waveguides and bent waveguides with a radius of $200\text{ }\mu\text{m}$, respectively.

The green, yellow and blue lines are for the cases of $W = 1.8\text{ }\mu\text{m}$, $1.9\text{ }\mu\text{m}$ and $2.0\text{ }\mu\text{m}$, respectively. **c, d** Second- (c) and fourth-order (d) dispersion at 1550 nm wavelength varying with W and H_1 when the radius of a single-mode rib Si_3N_4 nonlinear integrated waveguide is $400\text{ }\mu\text{m}$ for fabrication tolerance analysis.

Extended Data Table 1 | Parameters of spiral rib Si₃N₄ nonlinear integrated waveguides fabricated

Waveguide	Length (cm)	Rib gap (μm)	Slab width (μm)	Minimum spiral bending radius (μm)	Maximum spiral bending radius (μm)	Length of spiral unit (mm)	Chip size (mm ²)
WG 1	18	15	12	180	450	14.2	1 x 14
WG 2	56	50	30	165	450	7.4	3 x 29